Watari *et al. Earth, Planets and Space* (2021) 73:102
https://doi.org/10.1186/s40623-021-01422-3

Earth, Planets and Space

TECHNICAL REPORT

Open Access

Measurement of geomagnetically induced current (GIC) around Tokyo, Japan

Shinichi Watari[1*], Satoko Nakamura[2] and Yusuke Ebihara[3]

Abstract

We need a typical method of directly measuring geomagnetically induced current (GIC) to compare data for estimating a potential risk of power grids caused by GIC. Here, we overview GIC measurement systems that have appeared in published papers, note necessary requirements, report on our equipment, and show several examples of our measurements in substations around Tokyo, Japan. Although they are located at middle latitudes, GICs associated with various geomagnetic disturbances are observed, such as storm sudden commencements (SSCs) or sudden impulses (SIs) caused by interplanetary shocks, geomagnetic storms including a storm caused by abrupt southward turning of strong interplanetary magnetic field (IMF) associated with a magnetic cloud, bay disturbances caused by high-latitude aurora activities, and geomagnetic variation caused by a solar flare called the solar flare effect (SFE). All these results suggest that GIC at middle latitudes is sensitive to the magnetospheric current (the magnetopause current, the ring current, and the field-aligned current) and also the ionospheric current.

Keywords: Geomagnetically induced current (GIC), Equipment, Storm sudden commencement (SSC), Sudden impulse (SI), Geomagnetic storm, Bay disturbance, Solar flare effect (SFE), Magnetic cloud, Space weather

Introduction

Pulkkinen et al. (2012) noted that the magnitude of geoelectric fields induced by geomagnetic variations drastically drops below geomagnetic latitudes of approximately 50 degrees. However, several problems caused by geomagnetically induced current (GIC) have been reported from countries at low or middle geomagnetic latitudes. For example, the failure of transformers occurred in the Halfway Bush substation in New Zealand during the 6 November 2001 geomagnetic storm (Marshall et al. 2012). After the intense geomagnetic storms at the end of October 2003 (called the Halloween event), a problem with transformers was found in South Africa (Gaunt and Coetzee 2007). These events reported at low and middle latitudes are receiving increased attention. Recently, GIC measurements have been carried out in many countries, such as Brazil (Trivedi et al. 2007), Spain (Torta et al. 2012), Australia (Marshall et al. 2013), China (Liu et al. 2009), and Japan (Watari et al. 2009).

There are several methods of estimating GIC. For direct GIC measurement, clamp-type probes using magnetic sensors, such as Hall elements, flux gate sensors, and current transformer sensors, are usually attached to the line between the neutral point of a transformer and the ground. There is no commercial product dedicated to GIC measurement. Detailed information of the equipment is not always available, although it is useful for people who want to perform measurements. For example, detailed information of current probes was not given in the papers of Torta et al. (2012), Trivedi et al. (2007), and Liu et al. (2009).

The equipment used to measure GIC is basically composed of a current probe and a data logger. A computer with an analog to digital (AD) converter is also used as a data logger. Muchinapaya et al. (2018) reported a low-cost system to monitor GIC using an MBS Electrical model H20.3C Hall effect current sensor and a data logger based on a microcontroller board (Particle Electron

*Correspondence: watari@nict.go.jp
[1] National Institute of Information and Communications Technology, 4-2-1, Nukui-Kitamachi, Koganei, Tokyo 184-8795, Japan
Full list of author information is available at the end of the article

board with 12-bit AD converters and 2G/3G mobile network connection) with an SD memory card. In a case of 1-s sampling, their equipment produces approximately 1 GB of data in 1 year.

Marshall et al. (2013) used a Hall effect transducer (LEM model LT505-S) as a current probe and collected 1-min data using a supervisory control and data acquisition (SCADA) system of power network service providers. Only positive currents were measured initially and then the SCADA system was reconfigured to measure currents of both polarities.

Torta et al. (2012) recorded data of a Hall effect transducer with a sampling frequency of 1 kHz and synchronized the clock with Global Positioning System (GPS) time information. The stored data were transferred daily to a local server using the Universal Mobile Telecommunication System. One-minute GIC data were calculated to apply the fast Fourier transform (FFT) to the 1-kHz sampled data. They used 1-min geomagnetic data for their analysis. The temperature variation of the system was measured for temperature correction of the transducer using a Hall element.

Trivedi et al. (2007) used Hall detectors as a current probe and analyzed data with 1-min geomagnetic data. They did not report the details of their measurement system.

Liu et al. (2009) used a Hall sensor and an AD converter. They removed the power frequency (50 Hz in China) using a digital processing method involving a low-pass filter, a bandpass filter, and a 1-s integral unit before data were stored. To save memory, the recording procedure started when the measured value exceeded a predetermined threshold and continued until the measured value decreased to below the threshold.

Watari et al. (2009) measured GIC in Hokkaido, Japan using a clump-type current probe (HIOKI model 9279). The output signal was digitized by a 12-bit AD converter card of a personal computer for data acquisition. One-second data were obtained by averaging 1-ms data. Data were collected via the Integrated Services Digital Network. Clock information was synchronized with Japan Standard Time (JST) signal transmitted by low-frequency radio wave.

As indirect methods, magnetic or electric field measurements have been used to estimate GIC (Pulkkinen et al. 2007). The electric field is obtained by dividing the voltage measured between two electrodes in the ground by the distance between them. At the Kakioka Magnetic Observatory (KAK), two horizontal components of the electric field have been measured using two pairs of electrodes installed in both the north–south and east–west directions for more than 50 years (Fujii et al. 2015). Fujii et al. (2015) noted a long-term trend in the electric field data. However, its effect is small for variations with periods shorter than several tens of hours.

When the electric field data are available by observations or model calculations, GIC is given as

$$\mathrm{GIC} = \mathrm{a}E_x(t) + \mathrm{b}E_y(t), \tag{1}$$

where E_x and E_y are the north–south and east–west components of the local electric field, respectively. Coefficients a and b are the site-dependent system parameters, which depend on the topology and electrical characteristics of the power system. Weigel and Cilliers (2019) noted their frequency dependence.

In the frequency domain, the X- and Y-components of the electric field, $E_x(\omega)$ and $E_y(\omega)$, are calculated using magnetic field data:

$$E_x(\omega) = \frac{Z(\omega)}{\mu_0} B_y(\omega), \tag{2}$$

$$E_y(\omega) = -\frac{Z(\omega)}{\mu_0} B_x(\omega), \tag{3}$$

where μ_0 is the permeability of vacuum, $B_x(\omega)$ and $B_y(\omega)$ are the north–south and east–west components of the local geomagnetic field, respectively, and $Z(\omega)$ is the surface impedance. Nakamura et al. (2018) calculated the electric field by the 3-D finite-difference time-domain (FDTD) method assuming the sheet current from the observed geomagnetic field data. GIC of each substation is calculated by solving Kirchhoff's law with the electric field (Boteler and Pirjola 2017).

A differential magnetometer method (DMM) has been utilized to indirectly estimate GIC (Matandirotya et al. 2016; Hübert et al. 2020), where the Laboratory of Electromagnetic Innovations model LEMI-011 magnetometers were used. Matandirotya et al. (2016) recorded data using Onset Computer Corporation's HOBO data logger with a 12 V/8A battery and a voltage regulator. Hübert et al. (2020) used Earth Data's digitizer and sent data using a 4G mobile network modem.

Magnetic field variations are measured under a transmission line and compared with a measurement performed several hundred meters away from the transmission line. Assuming the Biot − Savart law, the magnetic field B, induced by GIC flowing through a power transmission line with height h is given as

$$B = \frac{\mu_0}{2\pi h}\mathrm{GIC}. \tag{4}$$

This technical report overviews the GIC measurement systems that have appeared in published papers, notes technical requirements for the direct measurement of GIC, and presents several examples of measured GICs.

In "Technical requirements for GIC measurement" section, we describe technical requirements for properly capturing the variation of GICs. We compare our GIC data with high-cadence geomagnetic and geoelectric field data observed at KAK. In "Measurement system" section, our measurement system and the locations of our measurements are introduced. In "Examples of measurement data" section, we present examples of GICs measured by our equipment.

Technical requirements for GIC measurement

The sampling rate of data is an important requirement to capture peak values associated with the rapid variations of GIC with the necessary frequency range to obtain a worst-case value of GIC. There is a trade-off between sampling rate and memory size. Substations are often located in remote areas and it is not easy to access the substations to collect data. We need to select a lower sampling rate to record data over longer periods without a remote access function.

The North American Electric Reliability Corporation (NERC) considered GIC as a quasi-DC current and recommended a sampling rate of 10 s or shorter for GIC measurement (NERC 2012, 2017). However, Grawe et al. (2018) noted that the high-frequency spectral content of the geomagnetic field can significantly influence the magnitude and direction of the induced surface electric field. They recommended electric field modeling using geomagnetic field measurements with a high cadence of shorter than 10 s for GIC estimation. Oyedokun et al. (2020) noted that approximately 98% of the energy in the GIC power spectrum is below 50 MHz from the analysis of 1-s cadence GIC data, while peak values of GIC were sometimes underestimated.

We sought a suitable sampling rate to capture peak values of GIC associated with rapid variations of the geomagnetic field, such as storm sudden commencements (SSCs) or sudden impulses (SIs). A failure of power grids associated with SSC was reported in New Zealand (Marshall et al. 2012). An increase in the sampling rate gives rise to a large amount of data. The problem of insufficient data storage capacity has been resolved by sending data in a real-time manner through an Internet-connected cellphone system.

Many types of geomagnetic variation are known to induce intense GIC at low and middle latitudes. One of the significant types is associated with SSCs or SIs (Kappenman 2003). Figure 1 shows 0.1-s data of the X-component (geographic north–south component) of the geomagnetic field observed at KAK (top left) and negative values of its time derivative (middle left) and of the Y-component (geographic east–west component) of the geoelectric field (E_y) observed at KAK (bottom left) when an SSC with an amplitude of 104 nT was observed at 18:33 UT (Universal Time) on 22 June 2015. This was the largest SSC since January 2012 when the 0.1-s recording started at KAK. Before this time, an analog high-pass filter, which passed frequencies with a period shorter than approximately 150 s, was applied to the 0.1-s data. The maximum value of $|dX/dt|$ was approximately 0.89 nT/s for this SSC.

The right panels summarize the frequency spectra of $X, -dX/dt$, and E_y, indicating broad enhancements at 0.1–0.4 Hz. This implies that, to properly capture the GIC for this event, a sampling frequency of at least 0.8 Hz is necessary according to the sampling theorem. The frequency spectrum of $-$ dX/dt also shows additional enhancement at a frequency of more than 0.4 Hz. The spectra of X and E_y roughly follow a power law at higher frequencies of up to 2 Hz. The power law indices are -0.97 and -0.91, respectively, as indicated by the red lines.

In addition to the transient phenomena such as SSCs, geomagnetic pulsations that fall into several categories depending on the period, ranging from 0.2 to 600 s, as shown in Table 1 (Saito 1969), are also expected to influence the GIC at middle and low latitudes. For example, Pc1 pulsations, in which the frequency ranges from 0.2 to 5 Hz, are often observed at middle and low latitudes (e.g., Althouse and Davis 1978; Nomura et al. 2011). High-cadence data make it possible to detect GICs associated with these pulsations.

There are some other requirements for GIC measurements in addition to the sampling rate. First, the polarity of the current must be measured to estimate the total GIC flowing into and out of the ground. Second, accurate clock information of the data is necessary to compare GIC data with other data, such as geomagnetic and/or geoelectric field data. Accurate clock information prevents a time shift among the data. For example, the estimations of a and b of Eq. (1) are affected by the time shift of the data. Signals from the Global Navigation Satellite System (GNSS), such as GPS, enable us to obtain accurate clock information for the equipment installed near the transformer.

Third, long-term stability of the measurements is necessary. To accomplish this, we need to monitor the equipment remotely.

Fourth, it is also necessary to remotely collect data in a near real-time manner. This resolves the limits of the data storage capacity and enables us to perform a nowcast. An Internet-connected cellphone system is a candidate for achieving this. For secure Internet connection with the measurement system, a secure protocol, such as the Secure Shell (SSH) protocol, is essential.

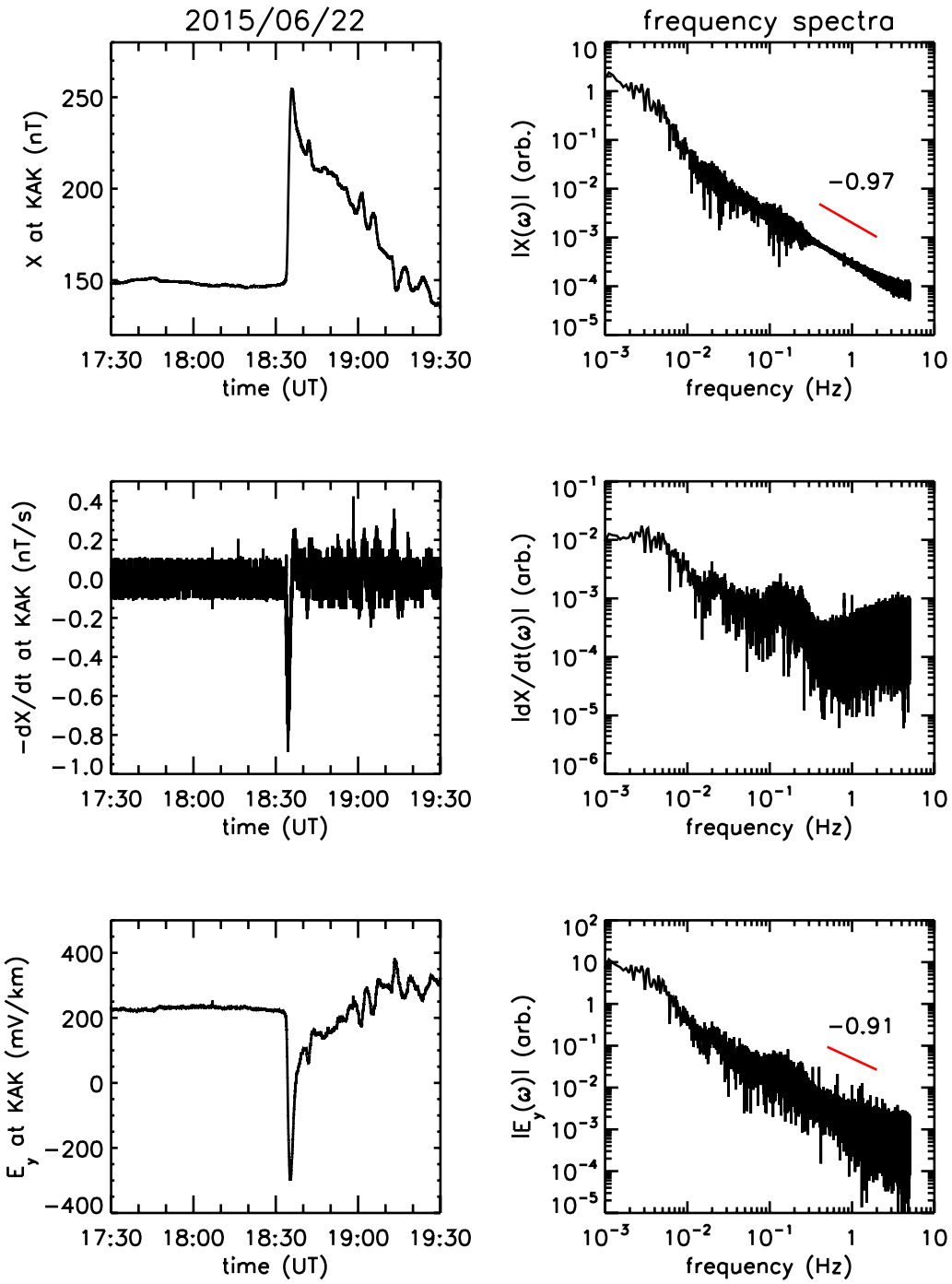

Fig. 1 0.1-s data of X-component geomagnetic field at KAK (top-left panel), negative values of its time derivative (middle-left panel), and Y-component geoelectric field at KAK (bottom-left panel) of the 22 June 2015 SSC and their frequency spectra (right panels)

Measurement system

We have developed a measurement system considering the above requirements. Figure 2 shows a block diagram of the equipment for our GIC measurement. We adopted a clamp-type current probe (HIOKI model CT6845) to measure current flowing in a line from the neutral point of a transformer to the ground. A larger clamp diameter is usually necessary to apply bar or circular conductors of transformer ground lines (Muchinapaya et al. 2018). The CT6845 probe has a clamp diameter of 50 mm and its

Table 1 Period ranges of pulsations of geomagnetic field

Notation	Period range (sec.)
Pc1	0.2–5
Pc2	5–10
Pc3	10–45
Pc4	45–150
Pc5	150–600
Pi1	1–40
Pi2	40–150

Table 2 Specifications of the CT6845 current probe

Parameter	Value
Rated current	±50 A for AC/DC
Max. allowable input	1000 A rms
Frequency range	DC to 100 kHz
Output voltage	4 mV/A
Measurable diameter	50 mm
Operating temperature	−40 °C to +85 °C

specifications are shown in Table 2. The CT6845 probe uses flux gate and current transformer sensors for magnetic detection to obtain a wide measurement frequency range (Ikeda 2017). The flux gate sensor has greater temperature stability and long-term stability than Hall elements. The output voltage of the probe is 4 mV/A and the input voltage of the 32-bit AD converter of the data logger (TIERRA TECNICA Ltd. model DCA323) is ± 2.5 V.

We set current flowing from the transformer to the ground as positive. An analog notch filter with a stopping frequency of 50 Hz was applied in front of the AD converter to remove the variation arising from the power lines. Data were sampled at 10 Hz and were recorded together with clock information synchronized with the GPS. We employed a mobile router (SUNCORPORATION model RX210) to remotely access the equipment and collect data through the mobile Internet connection using the SSH protocol.

Figure 3 shows the locations of substations SFS, STB, and SFJ, at which our instruments are operational as of 2020. Only the 500 kV power lines that are connected to these three substations are shown with the solid lines. 500 kV is the highest class of Japanese commercial power grid lines. The resistance of 500 kV lines is expected to be lower than that of lower voltage lines; thus, GIC with a large amplitude is expected to flow along 500 kV lines. A more detailed power grid model of the 500 kV lines is given by Nakamura et al. (2018). The plus sign indicates the location of the KAK observatory, where geomagnetic and geoelectric fields are recorded every 0.1 s. We started the measurements at substations STB and SFJ in February 2017 and those at substation STB in February 2018. SFJ is in the middle of east–west lines connecting the neighboring stations. STB faces SFS and are connected by an approximately north–south line with a length of approximately 163 km.

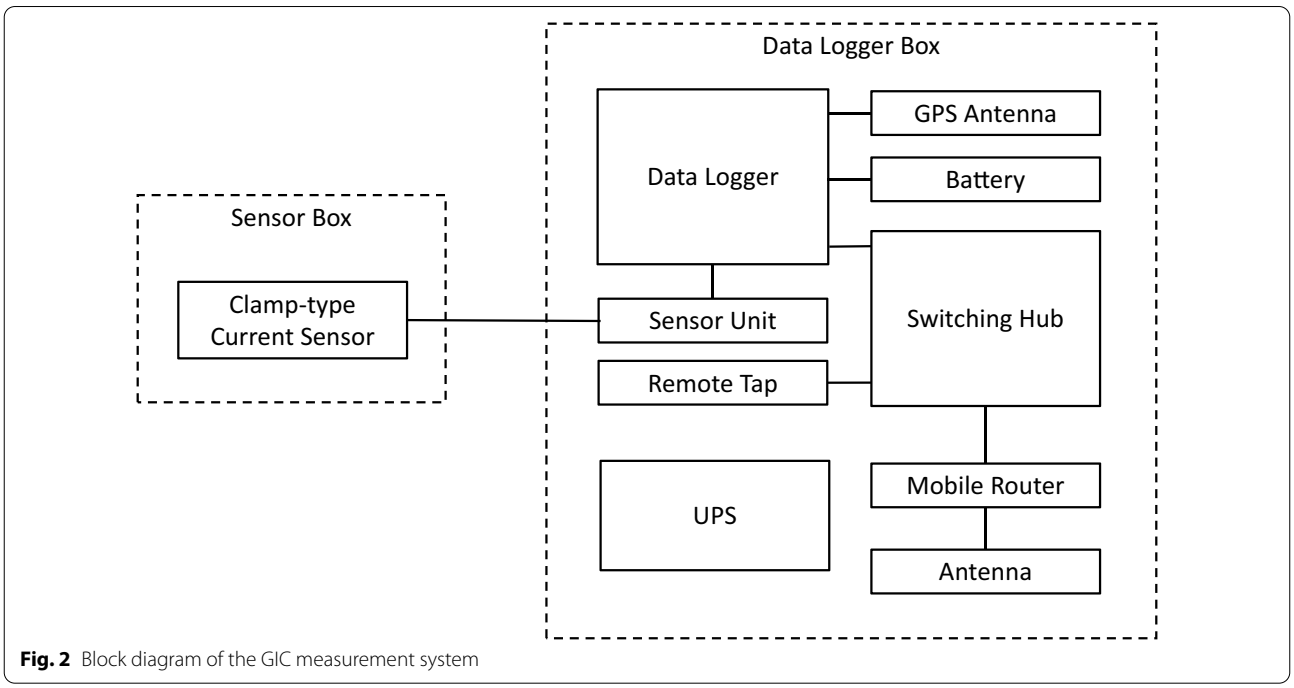

Fig. 2 Block diagram of the GIC measurement system

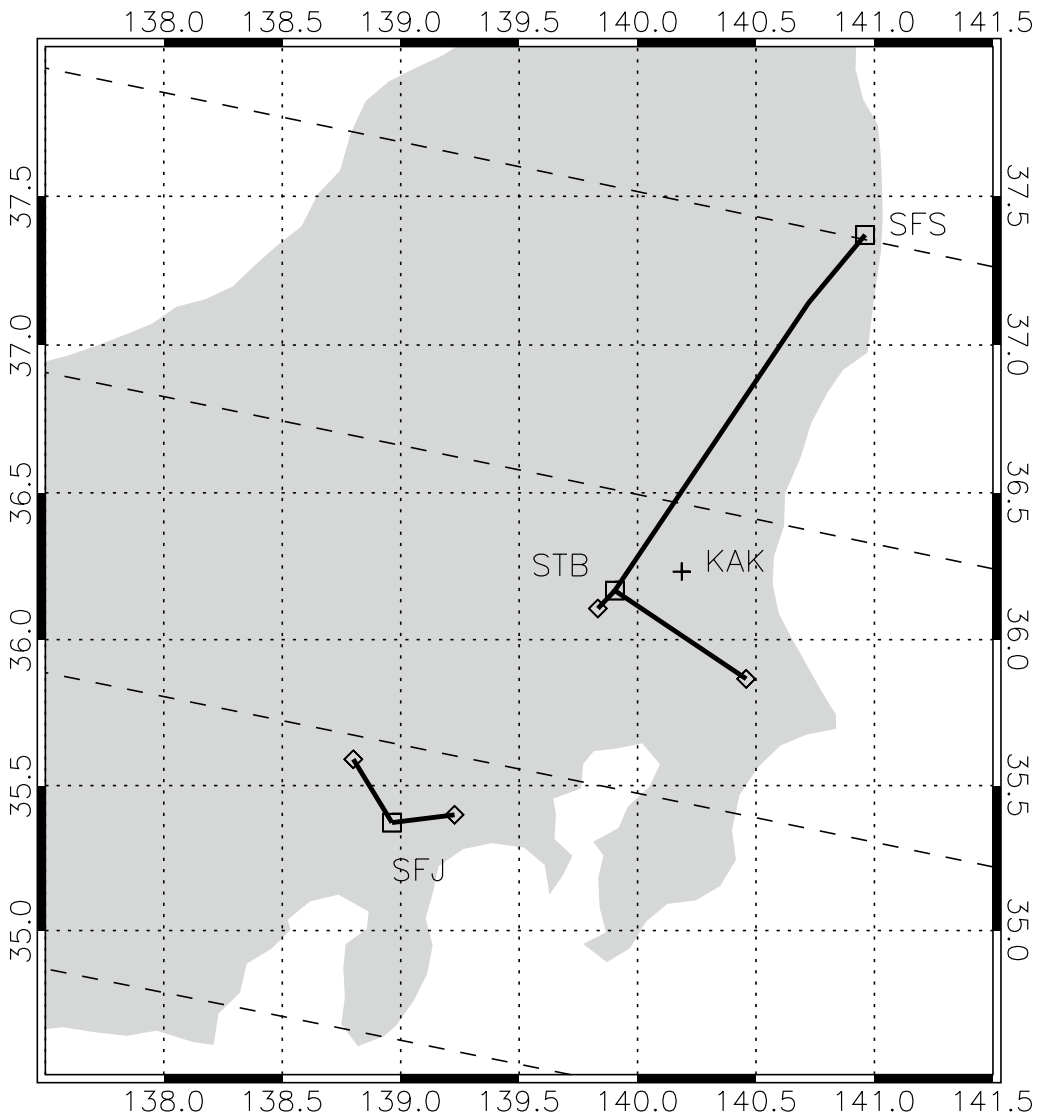

Fig. 3 Locations of GIC measurements of 500 kV lines. Squares show substations, where GIC measurements are performed, and diamonds show their neighbor substations. Solid lines show 500 kV lines between substations. The plus sign shows the location of the Kakioka Magnetic Observatory (KAK). The dashed lines show geomagnetic latitudes of 30º, 31º, 32º, and 33º, respectively

Examples of measurement data

We show examples of GICs associated with SSCs/SIs caused by interplanetary shocks, geomagnetic storms, bay disturbances caused by high-latitude aurora activities, and geomagnetic variations caused by a solar flare called the solar flare effect (SFE). Table 3 lists geomagnetic storms with minimum values of real-time Disturbance storm time (Dst) index of less than − 100 nT between February 2017 and August 2020 and the maximum values of GIC associated with them. Only three storms are listed in Table 3 because of the low solar activity during the minimum period of Cycle 24. Tables 4, 5, and 6, respectively, list SSCs/SIs, bay disturbances, and SFEs between February 2017 and August 2020 with the largest values of the horizontal (H−) component of the geomagnetic field reported from KAK and the maximum values of GIC associated with them. Note that large GICs were often observed in association with bay disturbances. The amplitudes can be as high as those associated with SSCs/SIs and geomagnetic storms. This implies that substorm activities can also cause large GICs even at middle latitudes.

Table 3 Geomagnetic storms with real-time Dst index of less than -100 nT and maximum GICs associated with them between February 2017 and August 2020

Order	Date & time (UT)	Type	Min. Dst (nT)	GIC (A)		
				SFJ	STB	SFS
1	2018/08/25 15:12	SG	−174	−3.38	2.42	NA
2	2017/05/27 15:30	SSC	−125	−2.30	−1.71	NA
3	2017/09/07 23:00	SSC	−124	NA	−3.65	NA

SSC: Storm Sudden Commencement; SG: Gradual Storm

Table 4 SSCs/SIs with largest values of H-component geomagnetic field reported from KAK and maximum GICs associated with them between February 2017 and August 2020

Order	Date & time (UT)	Type	Max. H (nT)	Max. dH/dt (nT/s)	GIC (A)		
					SFJ	STB	SFS
1	2017/07/16 05:59	SSC	70	0.75	3.21	2.65	NA
2	2017/06/16 08:33	SI[a]	−32	−0.20	−1.67	−0.85	NA
3	2017/05/15 09:15	SI[a]	−30	−0.20	−2.12	−1.23	NA
4	2017/07/02 10:29	SI	26	0.12	1.08	1.03	NA
5	2017/05/14 11:18	SI	−24	−0.10	−0.86	−0.87	NA
6	2017/06/11 14:39	SI	−22	−0.14	−1.10	−0.98	NA
7	2017/08/31 05:37	SSC[a]	22	0.41	NA	1.10	NA
8	2017/05/11 04:59	SI[a]	−21	−0.24	−1.34	−0.80	NA
9	2017/05/27 15:30	SSC	19	0.09	0.32	0.76	NA
	2017/06/03 12:34	SI[a]	−19	−0.18	−1.13	−0.90	NA
	2019/07/08 19:22	SI	19	0.16	NA	1.11	NA

SSC: Storm Sudden Commencement; SI: Sudden Impulse; NA: Not Available

[a] Negative variation

Table 5 Bay disturbances with largest values of H-component geomagnetic field reported from KAK and maximum GICs associated with them between February 2017 and August 2020

Order	Date & time (UT)	Type	Max. H (nT)	GIC (A)		
				SFJ	STB	SFS
1	2017/12/05 13:16	bp	57	1.20	1.86	NA
2	2018/08/26 15:48	bp	52	0.36	2.18	NA
3	2017/03/01 12:49	bp	49	1.14	1.21	NA
4	2017/02/01 14:49	bp	43	NA	NA	NA
5	2017/04/22 09:20	bp	39	NA	2.01	NA
6	2018/10/01 14:00	bp	39	1.45	1.14	−12.15
7	2017/07/22 08:06	b	−38	−1.69	−0.77	NA
8	2017/07/17 14:39	bp	36	−0.98	1.22	NA
9	2017/10/11 14:51	bp	36	NA	−3.09	NA
10	2017/07/09 09:36	bp	−34	−1.69	−1.06	NA
	2018/06/23 09:42	b	−34	−1.30	−0.90	NA

b: bay; bp: positive bay; NA: Not Available

Table 6 SFE with the largest value of H-component geomagnetic field reported from KAK and maximum GIC associated with it between February 2017 and August 2020

Date & time (UT)	Max. H (nT)	GIC (A)		
		SFJ	STB	SFS
2017/04/01 21:39	8	1.03	0.41	NA

Figure 4 shows GICs simultaneously observed at three substations, SFJ, STB, and SFS, associated with the 20 April 2018 storm. Positive values of GIC mean that the current flows from a transformer to the ground. The geographic north–south (X−) and geographic east–west (Y−) components of the geomagnetic and geoelectric fields observed at KAK are also presented.

The GIC data contain spikes with short durations. The corresponding spikes are not found in the magnetic and electric field data simultaneously acquired at KAK. Hence, we attribute the spikes to non-geophysical causes. These spikes affect the analysis of GIC, such as the calculation of the coefficients of Eq. (1). We removed the spikes simply by replacing GIC (t_n) with GIC (t_{n-1}) when $|\text{GIC}\ (t_n) - \text{GIC}\ (t_{n-1})|$ exceeded a threshold value, where GIC (t_n) and GIC (t_{n-1}) are the observed GICs at the n th and $n-1$ th time steps, respectively. We chose a threshold value of 0.5 A for GIC by trial and error. The geoelectric data at KAK also contains many spikes. We also removed the spikes of the geoelectric field in the same manner when their amplitude was greater than 10.5 V/km. In Fig. 4, we removed 193, 0, 174, 2468, and 948 spikes from the 1-day data of the GICs at SFJ, SFS, and STB, E_x, and E_y, respectively.

The amplitude of the background noise levels of the GIC data in Fig. 4 becomes small between ~ 16:00 UT and ~ 20:00 UT and between ~ 1:00 JST and ~ 5:00 JST. From this, we speculated that they are continuous noise associated with economic activities, including the frequent operation of electric trains. The amplitudes of the noise levels at SFJ and STB tend to be larger than that at SFS. The electromagnetic environment at SFJ is poor, because a train track using DC power and a town are several kilometers away from SFJ with trains running regularly between ~ 5:00 JST and ~ 24:00 JST. STB also suffers from urban electromagnetic noise, because it is located several tens of kilometers away from train tracks and a nearby city. SFS is probably located in a relatively quiet electromagnetic environment, because it is located approximately 50 km from the nearest large city and several kilometers from a train track using AC electric power.

A small negative excursion in the X-component magnetic field is identified, which corresponds to a small magnetic storm, with a minimum real-time Dst index of − 66 nT. The variation of the X-component magnetic field roughly traces the Dst variation, because KAK is one of the stations that contribute to the Dst index.

The GICs at STB and SFS varied oppositely. This can be understood in terms of the geometry of the power line. STB and SFS are connected by a line that extends in the north–east to south–west direction. It is speculated that the current tends to flow into SFS and away from STB when the geoelectric field is northward (or eastward). (Of course, the situation is not so simple, because power lines are connected from STB to the south–east and south–west, and power lines are connected from SFS to the north (Nakamura et al. 2018). Note that not all power lines are shown in Fig. 3.)

It is shown in Fig. 4 that the X-component geomagnetic field at KAK decreased monotonically between 4:00 UT and 10:00 UT, which corresponds to the main phase of the geomagnetic storm. During this interval, E_x and E_y at KAK increased to above the pre-storm level. The GIC at STB (SFS) decreased (increased). Around 10:20 UT and around 14:30 UT, positive excursions of GIC were observed at STB, whereas negative ones were observed at SFJ and SFS. The amplitude of the negative excursion at SFS is very large. As identified from the X-component geomagnetic field at KAK, the onsets of the positive bay disturbance took place around 9:50 UT and 14:20 UT. These moments roughly correspond to the onsets of the development of a westward auroral electrojet as inferred from the real-time AL index. Thus, the positive (negative) excursions of GIC around 10:20 UT and around 14:30 UT at STB (SFS) are probably associated with substorm expansion.

The correlation between the GIC at SFJ and the electric field at KAK is poor in comparison with that for the other substations. Nakamura et al. (2018) have attributed this to uneven ground conductivities associated with the active volcanic zone near SFJ. Another possibility is the configuration of power lines connecting neighboring substations.

Figure 5 shows the GIC variations at a 0.1-s sampling rate during the SSC on 16 July 2017, together with geomagnetic fields and negative values of their time derivatives, and geoelectric fields at KAK. This SSC is the largest one in our observation and the only event with the maximum H-component geomagnetic field larger than 50 nT. The SSC with an amplitude of 70 nT started at 5:59 UT. The maximum value of $|dX/dt|$ is approximately 0.88 nT/s. The peak-to-peak amplitudes are ~ 315 mV/km in the west component and ~ 63 mV/km in the south component. GIC at SFJ clearly shows double peaks, whereas the first peak is somewhat broad at STB. These variations are probably due to the superposition of

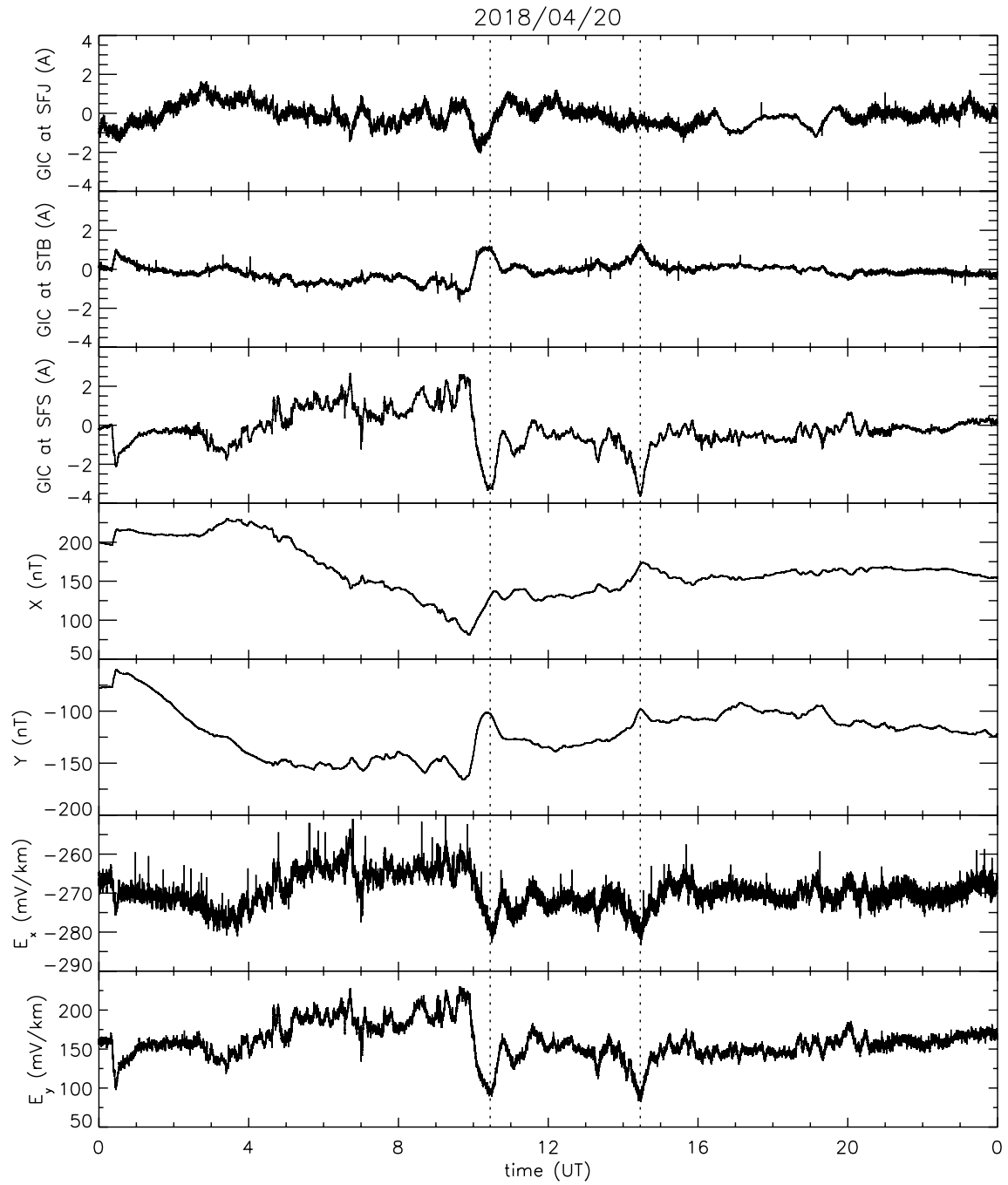

Fig. 4 0.1-s data of GICs at SFJ, STB, and SFS and X- and Y-components of geomagnetic and geoelectric fields at KAK of the 20 April 2018 geomagnetic storm. Vertical dotted lines show the excursions of GICs noted in the text

the DL field (directly caused by the intensification of the magnetopause current) and the DP field (directly caused by the ionospheric current) (Araki 1994). At present, the number of ground magnetic field data available on the web is limited. We will confirm the cause of the double peaks in the future.

Figure 6 shows the effect of the sampling intervals on the maximum value of GIC using the data shown in Fig. 5. We calculated the resampled data $\mathrm{GIC}^{i}_{\Delta T\,\mathrm{sec.}}$ from the 0.1-s sampled data $\mathrm{GIC}^{j}_{0.1\mathrm{sec.}}$:

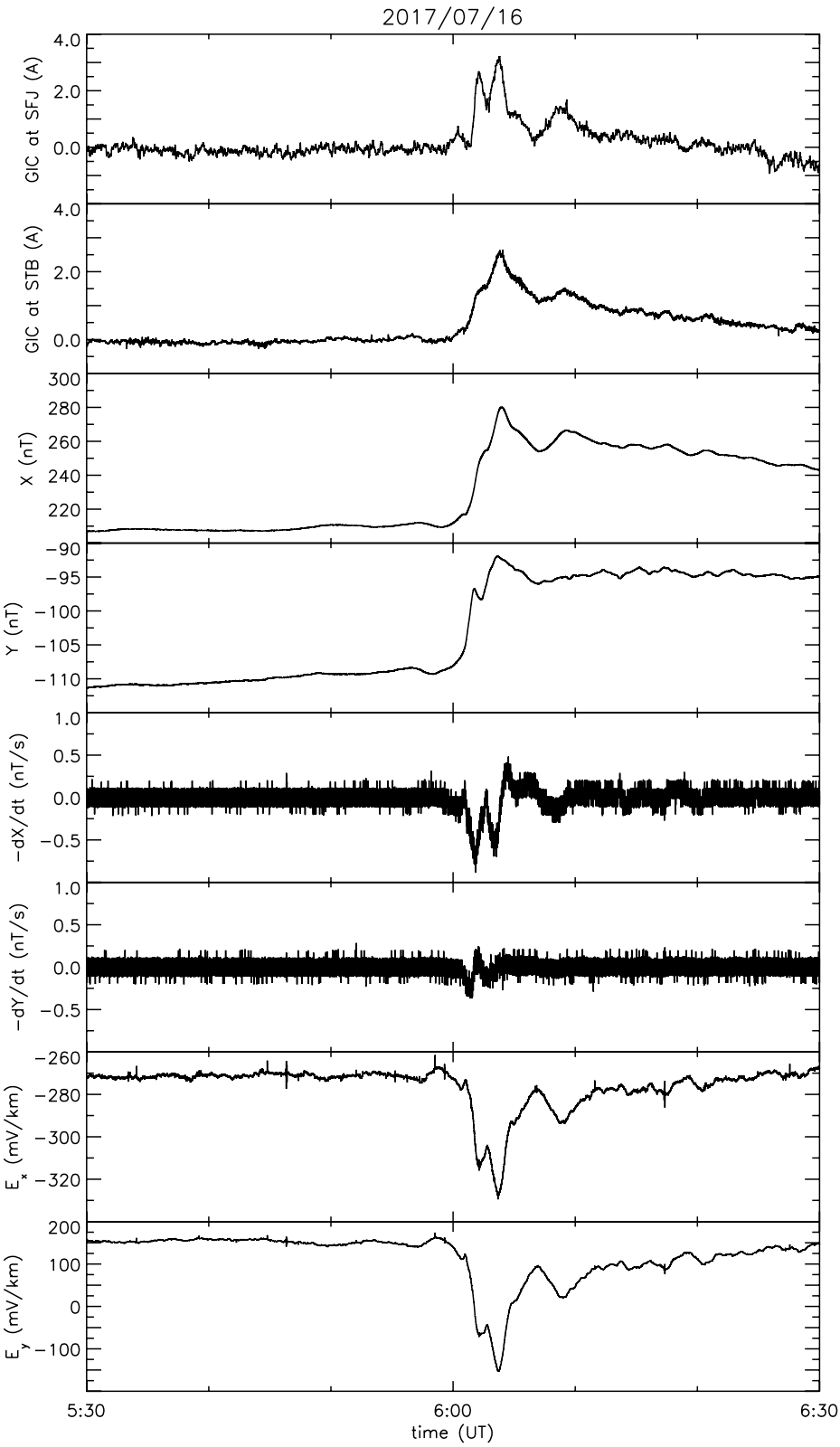

Fig. 5 0.1-s data of X- and Y-components of geomagnetic field at KAK and negative values of their time derivatives, and of X- and Y-components of geoelectric field at KAK associated with the 16 July 2017 SSC

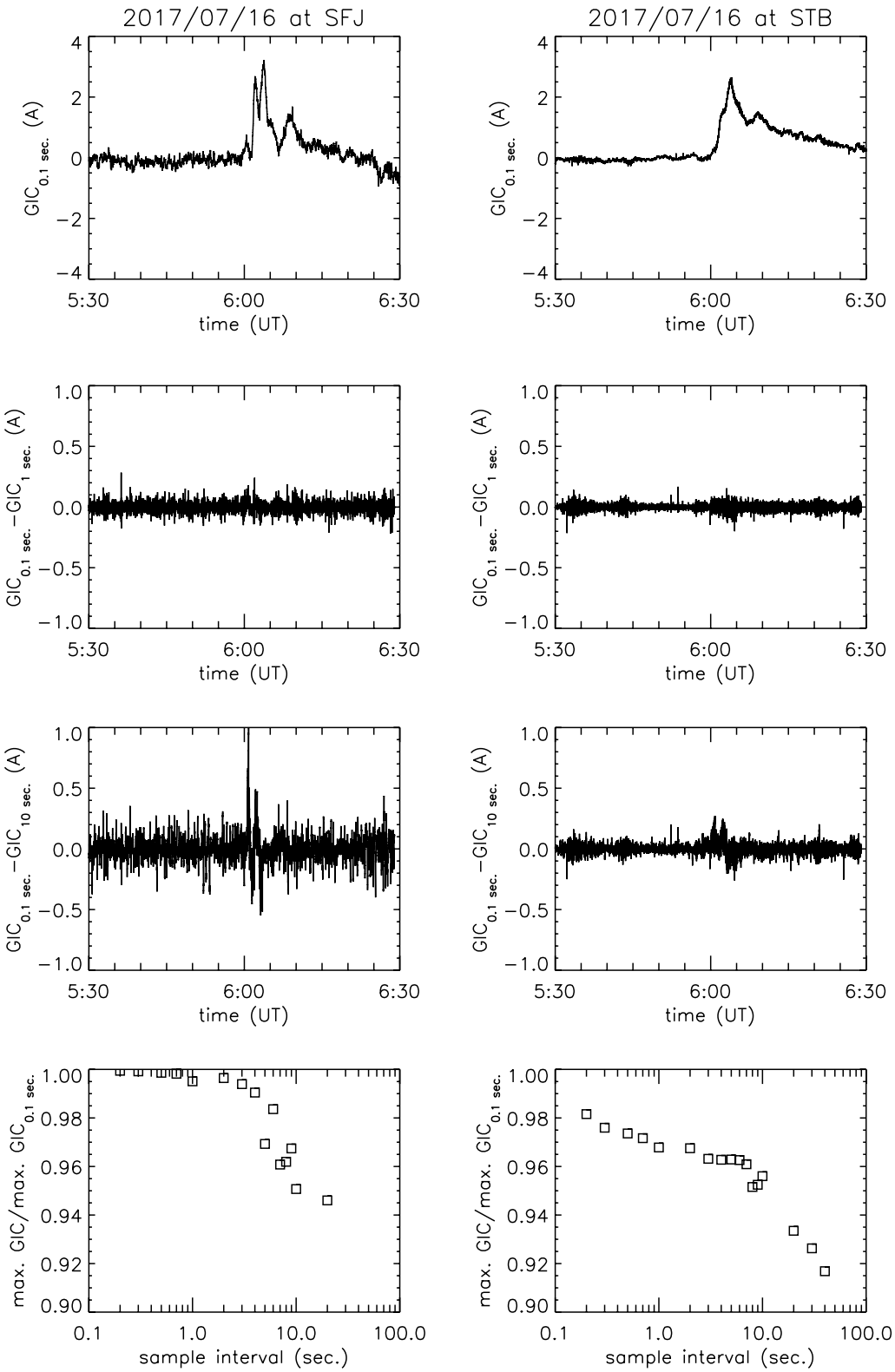

Fig. 6 GIC at SFJ and STB associated with the 16 July 2017 SSC. The top panel shows the raw GIC data with 0.1-s sampling. The second- and third-row panels show the differences between data sampled every 0.1 s and the 1-s resampled data and the differences between the data sampled every 0.1 s and the 10-s resampled data, respectively. The bottom panels show the ratio of the maximum GIC of the resampled data for the given sample interval to that of the 0.1-s sampled data as a function of the sample intervals

$$\mathrm{GIC}^{i}_{\Delta T\,\mathrm{sec.}} = \frac{0.1}{\Delta T} \sum_{j=(\Delta T/0.1)i-\Delta T/0.2+1}^{(\Delta T/0.1)i+\Delta T/0.2} \mathrm{GIC}^{j}_{0.1\,\mathrm{sec.}}, \quad (5)$$

where ΔT is a resampling interval.

The top panels of Fig. 6 show the GIC sampled at 0.1 s intervals. The second-row panels show the differences between the GIC data sampled every 0.1 s and the 1-s resampled data. The third-row panels show the differences between the GIC data sampled every 0.1 s and the 10-s resampled data. The bottom panels show the ratio of the maximum GIC of the resampled data with a given sample interval to that of the 0.1-s sampled data as a function of the sample interval. The ratio is almost unity at SFJ and is greater than 0.97 at STB when the sample interval being smaller than 0.7 s. The ratio decreases as increasing the sampling interval. These results suggest that a sample interval shorter than 1–2 s is suitable.

Figure 7 shows the frequency spectra of GICs at SFJ and STB for the 16 July 2017 SSC. At SFJ, the frequency spectrum roughly follows a power law between 0.1 and 2 Hz and becomes almost flat above 2 Hz. The power law index is − 1.59, as indicated by the red line, and there is a slight hump around 0.1 Hz. On the other hand, at STB, the frequency spectrum roughly follows a power law between 0.01 and 0.5 Hz and becomes almost flat above 0.5 Hz. The power law index is − 0.94 and no clear hump is found around 0.1 Hz. This may be attributed to the difference in underground conductivity structures.

Figure 8 shows an example of GIC associated with bay disturbances on 5 December 2017, together with the geomagnetic and geoelectric fields. Two distinct bay disturbances were observed around 14:00 UT and 17:00 UT. The onsets of the bay disturbances coincided with the onsets of the development of a westward auroral electrojet as inferred from the provisional AE index. GIC at STB shows a peak around 14:00 UT, whereas GIC at SFJ shows a dip around 14:00 UT. GIC at SFJ shows double peaks around 13:50 UT and 14:20 UT. For the bay disturbance around 17:00 UT, GIC at SFJ showed a definite peak, while GIC at STB showed a small variation.

Figure 9 shows an example of GIC associated with SFE caused by the M4.4/1F flare on 1 April 2017, together with the geomagnetic and geoelectric fields. When the flare reached its maximum phase at 21:48 UT, the GICs showed corresponding variations. X-ray radiation

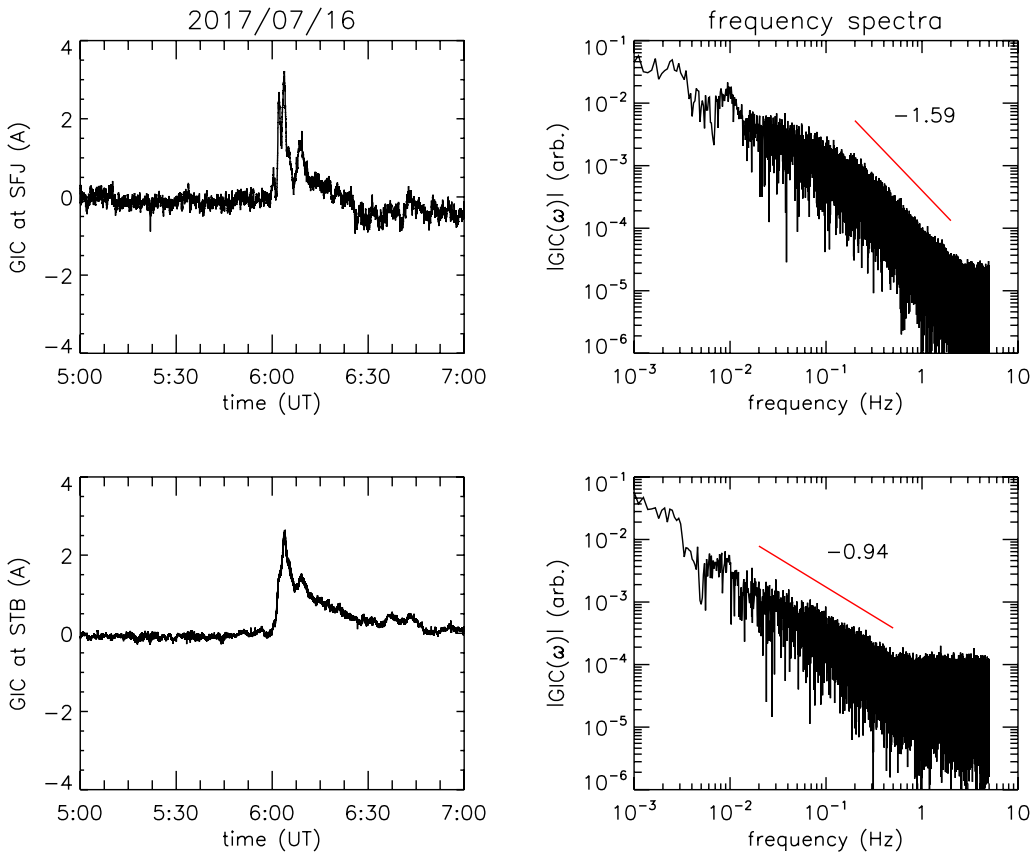

Fig. 7 0.1-s data of GICs at SFJ and STB of the 16 July 2017 SSC and their frequency spectra

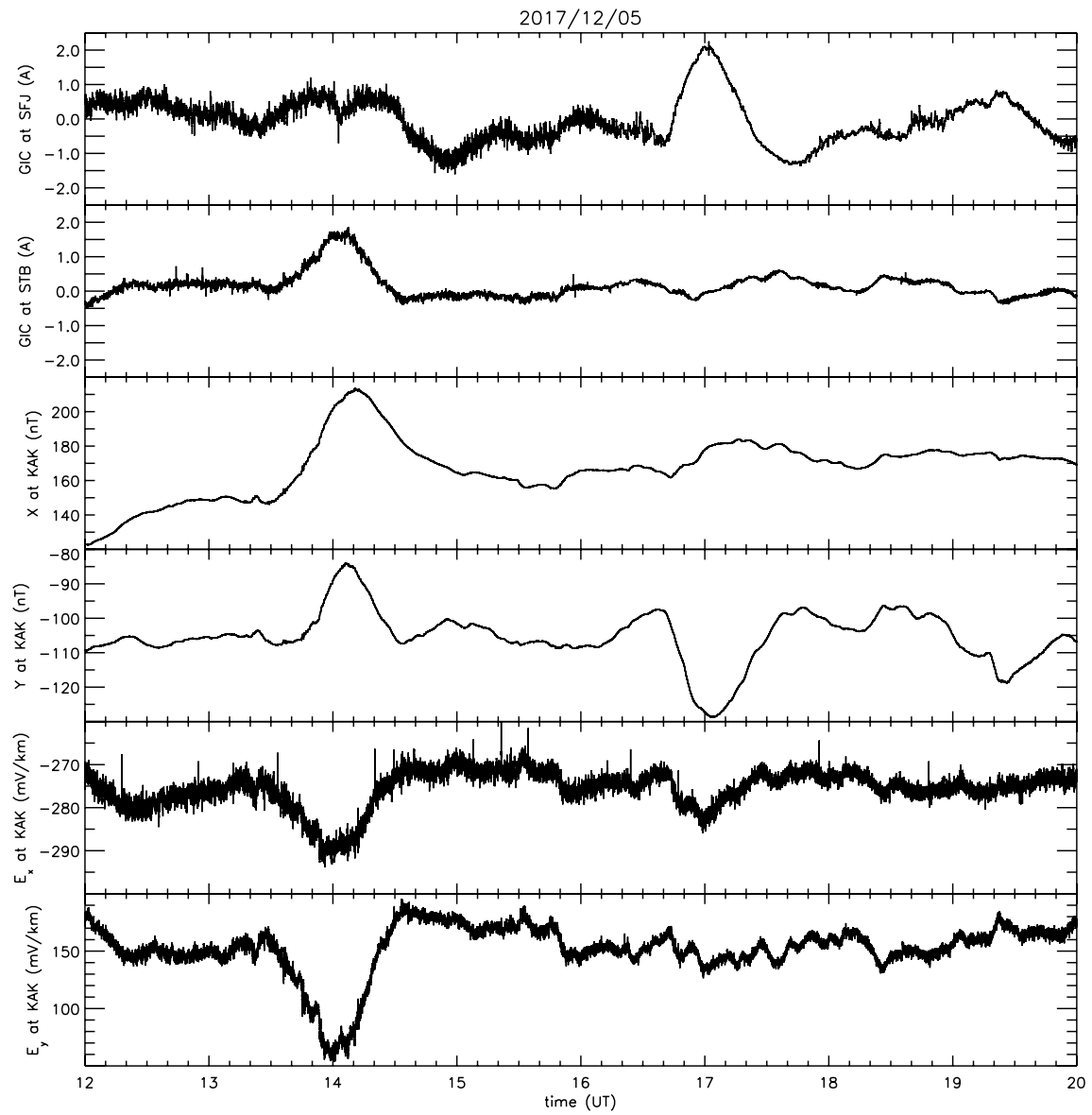

Fig. 8 GIC at SFJ and STB, and X- and Y-components of geomagnetic and geoelectric fields at KAK associated with bay disturbances on 5 December 2017

emitted by a solar flare increases ionization in the D and E layers of the ionosphere. This increases the conductivity of the ionosphere and makes ionospheric currents flow easily. The increased currents of the ionosphere produce a variation of the geomagnetic field called the SFE. This is an example of GIC caused by a solar flare.

Figure 10 shows an example of the GIC associated with the intense geomagnetic storm on 7–8 September 2017, together with the geomagnetic and geoelectric fields. Here, 1-min GIC data of SFJ are used because of a problem with the equipment. The real-time Dst index reached the minimum value of − 124 nT at 2:00 UT on 8 September 2017. An SSC was recorded at 23:00 UT on 7 September 2017 at KAK. After that, the X-component geomagnetic field at KAK shows a negative excursion between ~ 23:00 UT on 7 September and ~ 3:00 UT on 8 September, which is associated with the storm and is most likely caused by the intensification of the storm-time ring current. Two local minima are found at 23:30 UT and 0:40 UT. GIC at STB also shows two local minima at 23:30 UT and 0:40 UT. On the other hand, the local maxima of E_y at KAK at 23:30 UT and 0:40

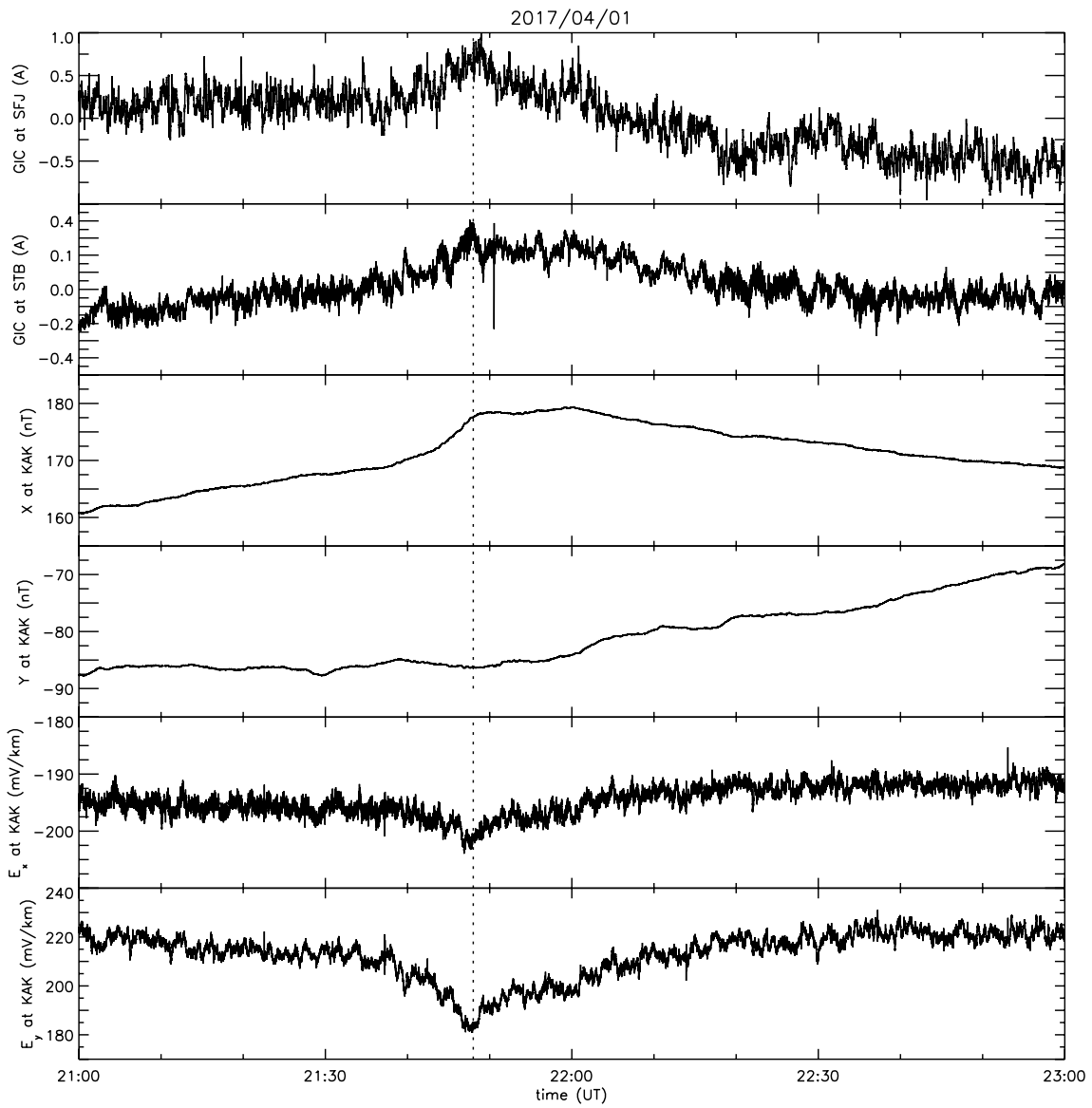

Fig. 9 GIC at SFJ and STB, and X- and Y-components of geomagnetic and geoelectric fields at KAK associated with the SFE caused by the M4.4/1F flare on 1 April 2017. The dotted vertical line shows the time of the maximum phase of the flare

UT coincide well with the local minima of GIC at STB. Roughly speaking, E_y at KAK is inversely proportional to the X-component geomagnetic field at KAK. Since the geoelectric field is well expressed by the convolution of the geomagnetic field with a reasonable lithospheric conductivity (Cagniard 1953; Pirjola 1985; Viljanen and Pirjola 1989; Love and Swidinsky 2014), these results imply that the GIC cannot be simply understood as the instantaneous time derivative of the geomagnetic field, but is also its convolution.

Figure 11 shows the longitudinally symmetric disturbance for horizontal component (SYM-H) index, which is essentially the same as the Dst index with 1-min time resolution (Iyemori et al. 2010), and solar wind parameters of the 7 September 2017 geomagnetic storm. This storm was caused by the magnetic cloud from the X9.3/2B flare (S08W33), which occurred in the NOAA active region 12,673 at 12:02 UT on 6 September 2017 and accompanied an asymmetric full halo coronal mass ejection (CME). The solar wind parameters were obtained from the NASA/GSFC OMNI data. Their time values are shifted from the location of the upstream observation by the spacecraft to the bow shock nose. We have to pay attention to ensure that an approximately

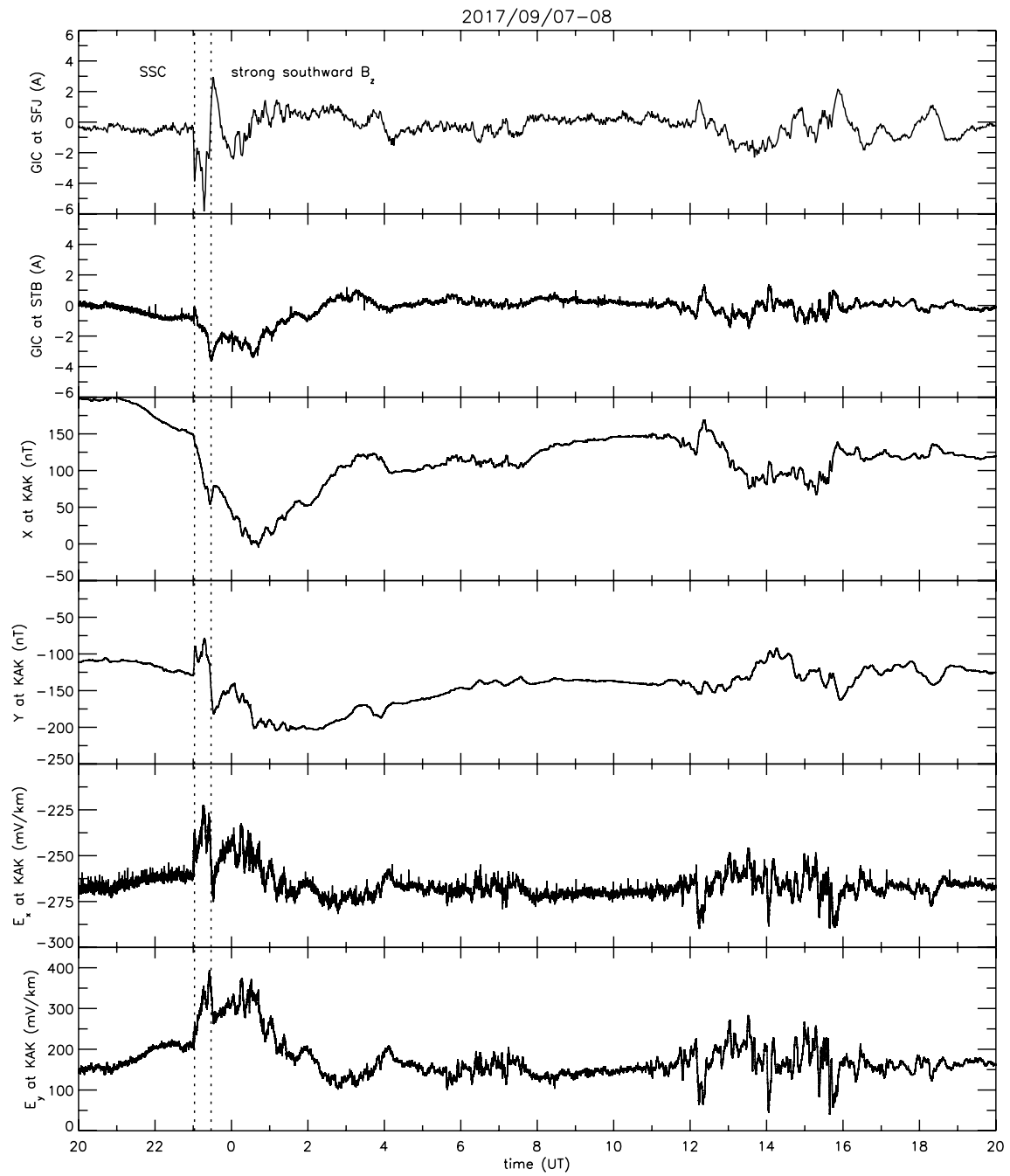

Fig. 10 One-minute GIC data at SFJ, 0.1-s GIC data at STB, and X- and Y-components of geomagnetic and geoelectric fields at KAK of the 7–8 September 2017 geomagnetic storm. The two dotted vertical lines show the time of the SSC and the start of the strong southward B_z shown in Fig. 11

10-min time lag still appears between the increase in the solar wind dynamic pressure and the increase in the SYM-H index. With the consideration of the time lag, the GIC variations can be understood as follows. The sudden increase in the solar wind dynamic pressure triggered the abrupt change in the GICs at SFJ and STB at 23:00 UT. Together with the prolonged southward component of the interplanetary magnetic field (IMF), the magnetospheric convection is strongly enhanced, giving rise to the development of the storm-time ring current (Burton

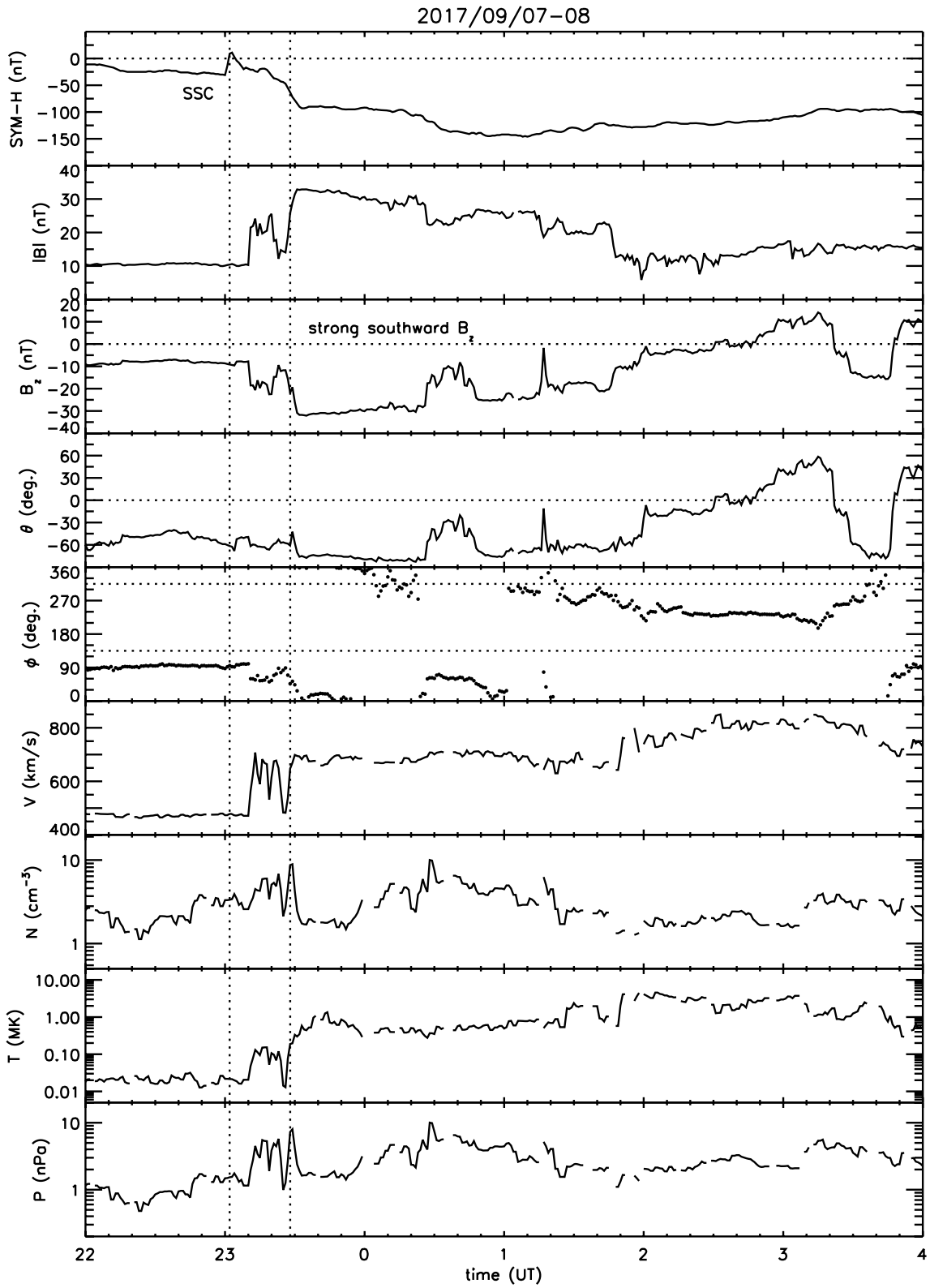

Fig. 11 One-minute data of SYM-H index and solar wind parameters of the 7–8 September 2017 geomagnetic storm. The two dotted vertical lines show the time of the SSC and the start of the strong southward B_z

et al. 1975; Ebihara and Ejiri 2003). The southward IMF increased from about −10 nT to about −30 nT, which caused further enhancement of the magnetospheric convection. The increase in the magnetospheric convection gives rise to an increase in the storm-time ring current on the nightside and a decrease in the dawn-noon sector (Ebihara and Ejiri 2000; Ebihara et al. 2002; Hashimoto et al. 2002; Brandt et al. 2002). Fresh ions originating from the nightside plasma sheet entered the inner magnetosphere, while the ions that pre-existed in the dawn-noon sector flowed out from the inner magnetosphere. Japan was situated in the dawn-noon sector; thus, the contribution from the ring current was temporally weakened. Consequently, the X-component geomagnetic field at KAK shows a small positive excursion after 23:30 UT. The rapid increase in the X-component geomagnetic field at KAK around 23:20 UT is considered to result in a substantial decrease in E_y at KAK in accordance with the induction (Love and Swidinsky 2014). The decrease in E_y at KAK resulted in an increase in GIC at SFJ with a time scale of a few minutes. GIC at SFJ was anti-correlated with E_y at KAK as shown in Fig. 5.

The GIC variation at SFJ is not simply related to the geoelectric field at KAK (Nakamura et al. 2018). Nakamura et al. (2018) assumed the electric conductivities of the air, the seawater, the sediment layer, and the basement rock layer and calculated the electric field by the 3-D FDTD method. This problem might be resolved by incorporating the localized lithospheric conductivity into this simulation.

Summary

We overviewed the GIC measurement systems in previously published papers. We noted technical requirements for the direct measurement of GIC and developed our equipment considering the following.

1. A sampling interval shorter than 1–2 s is suitable, as shown in Fig. 6. Considering that geomagnetic field data with a cadence of 1 s or higher have become available, a sampling rate of more than 1 Hz is recommended for GIC measurement to track detailed peaks or rapid variations of GIC. This also enables us to compare GIC data with high-cadence geomagnetic or geoelectric field data.
2. Measurement of the polarity of the current is required to determine the flow direction of GIC. The polarity of a current flow is useful for analysis that considers the configuration of power lines.
3. Accurate clock information synchronized with the GNSS, such as the GPS, is required to compare GIC data with other data. This is important when we use data with higher time resolution.
4. An Internet connection using a cellphone system is required to collect GIC data from a substation in a real-time manner and to control the equipment remotely. The problem of insufficient data storage space for a high sampling rate can be resolved by collecting data via the Internet connection.

We presented several examples of GIC data obtained by our equipment in this technical report. Despite the minimum period of Cycle 24, we succeeded in observing GIC at middle latitudes associated with various geomagnetic disturbances, such as SSCs/SIs, geomagnetic storms including a storm caused by abrupt southward turning of the strong IMF associated with a magnetic cloud, bay disturbances, and the SFE.

These observations suggest that GIC at middle latitudes is sensitive to the magnetospheric current (the magnetopause current, the ring current, and the field-aligned current) and also the ionospheric current.

Abbreviations

AC: Alternating current; AD: Analog to digital; CME: Coronal mass ejection; DC: Direct current; DMM: Differential magnetometer method; Dst: Disturbance storm time (index); FDTD: Finite-difference time domain; FFT: Fast Fourier transform; GIC: Geomagnetically induced current; GNSS: Global Navigation Satellite System; GPS: Global positioning system; GSFC: Goddard space flight center; IMF: Interplanetary magnetic field; JST: Japan standard time; KAK: Kakioka magnetic observatory; NASA: National aeronautics and space administration; NERC: North American Electric Reliability Corporation; NOAA: National Oceanic and Atmospheric Administration; SCADA: Supervisory control and data acquisition; SFE: Solar flare effect; SI: Sudden impulse; SSC: Storm sudden commencement; SSH: Secure Shell; SYM-H: Longitudinally symmetric disturbance field for horizontal (H) component; TEPCO: Tokyo Electric Power Company Holdings; UT: Universal time.

Acknowledgements

We thank TEPCO Power Grid for the permission and support of our GIC measurement at its substations. We also thank the Kakioka Magnetic Observatory, Japan Meteorological Agency for providing the list of geomagnetic disturbances and 0.1-s data of geomagnetic and geoelectric fields, the NASA/GSFC OMNI data for solar wind parameters, and the World Data Center for Geomagnetism, Kyoto for the real-time Dst, real-time AL, provisional AE, and SYM-H indices. We acknowledge the help of TIERRA TECNICA Ltd. in the installation of the equipment. This work was supported by a Grant-in-Aid for Scientific Research on Innovative Areas, JSPS KAKENHI Grant Number 15H05815. This work was also supported by Research Institute for Sustainable Humanosphere (RISH), Kyoto University, Mission Research 5–3.

Authors' contributions

SW contributed developing the GIC measurement equipment, analyzed the GIC data, and prepared this manuscript. SN contributed collecting GIC data from the substations. YE contributed collecting GIC data from the substations, organized this GIC project, and negotiated with TEPCO (Tokyo Electric Power Company Holdings) Power Grid about the GIC measurement. All authors read and approved the final manuscript.

Funding

This work was supported by a Grant-in-Aid for Scientific Research on Innovative Areas, JSPS KAKENHI Grant Number 15H05815.

Availability of data and materials

The list of geomagnetic disturbances and 0.1-s data of geomagnetic and geoelectric fields were provided by the Kakioka Magnetic Observatory, Japan

Meteorological Agency (https://www.kakioka-jma.go.hp/obddata/metadata/en). Real-time Dst, real-time AL, provisional AE, and SYM-H indices were taken from the World Data Center for Geomagnetism, Kyoto (http://wdc.kugi.kyoto-u.ac.jp/wdc/Sec3.html). Solar wind parameters were taken from the NASA/GSFC OMNI data (https://spdf.gsfc.nasa.gov/pub/data/omni/high_res_omni/). The measurements of GIC at substations SFJ, STB, and SFS were conducted in cooperation with the electric company. Please contact SW or YE for detailed information about the GIC data.

Declarations

Ethics approval and consent to participate
Not applicable.

Consent for publication
Not applicable.

Competing interests
The authors declare that they have no competing interests.

Author details
[1]National Institute of Information and Communications Technology, 4-2-1, Nukui-Kitamachi, Koganei, Tokyo 184-8795, Japan. [2]Institute for Space-Earth Environmental Research, Nagoya University, Furo-cho, Chikusa-ku, Nagoya 464-8601, Japan. [3]Research Institute for Sustainable Humanosphere, Kyoto University, Gokasho, Uji City, Kyoto 611-0011, Japan.

Received: 11 August 2020 Accepted: 23 April 2021
Published online: 07 May 2021

References

Althouse EL, Davis JR (1978) Five-station observations of Pc 1 micropulsation propagation. J Geophys Res 83(A1):132–144. https://doi.org/10.1029/JA083iA01p00132

Araki T (1994) A physical model of geomagnetic sudden commencement. In: Engebretson MJ, Takahashi K, Scholer M (eds) Solar wind sources of magnetospheric ultra-low-frequency waves. Geophys Monograph, vol 81. AGU, Washington DC, pp 183–200. https://doi.org/10.1029/GM081p0183

Boteler DH, Pirjola J (2017) Modeling geomagnetically induced currents. Space Weather 15(1):258–276. https://doi.org/10.1002/2016SW001499

Brandt PC, Mitchell DG, Ebihara Y, Sandel BR, Roelof EC, Burch JL, Demajistre R (2002) Global IMAGE/HENA observations of the ring current: examples of rapid response to IMF and ring current-plasmasphere interaction. J Geophys Res 107(11):12-1-SMP 12-12. https://doi.org/10.1029/2001JA000084

Burton RK, McPherron RL, Russell CT (1975) An empirical relationship between interplanetary conditions and Dst. J Geophys Res 80(31):4204–4214. https://doi.org/10.1029/JA080i031p04204

Cagniard L (1953) Basic theory of the magneto-telluric method of geophysical prospecting. Geophysics 18:605–635. https://doi.org/10.1190/1.1437915

Ebihara Y, Ejiri M (2000) Simulation study on the fundamental property of storm-time ring currents. J Geophys Res 105(A7):15843–15859. https://doi.org/10.1029/1999JA900493

Ebihara Y, Ejiri M, Nilsson H, Sandahl I, Milillo A, Grande M, Fennell JF, Roeder JL (2002) Statistical distribution of the storm-time proton ring current: POLAR measurements. Geophys Res Lett 29(20):1969. https://doi.org/10.1029/2002GL015430

Ebihara Y, Ejiri M (2003) Numerical simulation of the ring current: review. Space Sci Rev 105(1–2):377–452. https://doi.org/10.1023/A:1023905607888

Fujii I, Ookawa T, Nagamachi S, Owada T (2015) The characteristics of geoelectric fields at Kakioka, Kanoya, and Memanbetsu inferred from voltage measurements during 2000 to 2011. Earth Planets Space 67:62. https://doi.org/10.1186/s40623-015-0241-z

Gaunt CT, Coetzee G (2007) Transformer failures in regions incorrectly considered to have low GIC-risk. Paper presented at 2007 IEEE Lausanne Power Tech Conference, Lausanne, Switzerland, 1–5 July 2007, pp 807–812. Doi: https://doi.org/10.1109/PCT.2007.4538419.

Grawe MA, Makela JJ, Butala MD, Kamalabadi F (2018) The impact of magnetic field temporal sampling on modeled surface electric fields. Space Weather 16:1721–1739. https://doi.org/10.1029/2018SW001896

Hashimoto KK, Kikuchi T, Ebihara Y (2002) Response of the magnetospheric convection to sudden interplanetary magnetic field changes as deduced from the evolution of partial ring currents. J Geophys Res 107(A11):1337. https://doi.org/10.1029/2001JA009228

Hübert J, Beggan CD, Richardson GS, Martyn T, Thomson AWP (2020) Differential magnetometer measurements of geomagnetically induced currents in a complex high voltage network. Space Weather 18(4):e2019SW002421. https://doi.org/10.1029/2019SW002421

Iyemori T, Takeda M, Nose M, Odagi Y, Toh H (2010) Mid-latitude geomagnetic indices ASY and SYM for 2009 (Provisional). Internal report of data analysis center for geomagnetism and space magnetism, Kyoto University, Japan. http://wdc.kugi.kyoto-u.ac.jp/aeasy/asy.pdf. Accessed 28 Mar 2021

Ikeda K (2017) AC/DC current probe CT6844/CT6845/CT6846. HIOKI Technical Notes 3(1):1–12

Kappenman JG (2003) Storm sudden commencement events and the associated geomagnetically induced current risks to ground-based systems at low-latitude and midlatitude locations. Space Weather 1(3):1016. https://doi.org/10.1029/2003SW000009

Liu C, Liu L, Yang Y (2009) Monitoring and modeling geomagnetically induced currents in power grids of China. Paper presented at 2009 Asia-Pacific Power and Energy Engineering Conference, Wuhan, China, 27–31 March 2009. Doi: https://doi.org/10.1109/APPEEC.2009.4918502.

Love JJ, Swidinsky A (2014) Time causal operational estimation of electric fields induced in the Earth's lithosphere during magnetic storms. Geophys Res Lett 41:2266–2274. https://doi.org/10.1002/2014GL059568

Marshall RA, Dalzell M, Waters CL, Goldthorpe P, Smith EA (2012) Geomagnetically induced currents in the New Zealand power network. Space Weather 10(8):S08003. https://doi.org/10.1029/2012SW000806

Marshall RA, Gorniak H, Walt TVD, Waters CL, Sciffer MD, Miller M, Dalzell M, Daly T, Pouferis G, Hesse G, Wilkinson P (2013) Observations of geomagnetically induced currents in the Australian power network. Space Weather 11(1):6–16. https://doi.org/10.1029/2012SW000849

Matandirotya E, Cilliers PJ, Van Zyl RR, Oyedokun DT, de Villiers J (2016) Differential magnetometer method applied to measurement of geomagnetically induced currents in Southern African power networks. Space Weather 14(3):221–232. https://doi.org/10.1002/2015SW001289

Muchinapaya A, Gaunt CT, Oyedokun DTO (2018) Design of a low-cost system to monitor geomagnetically induced currents in transformer neutrals. Paper presented at 2018 IEEE PES/IAS PowerAfrica, Cape Town, South Africa, 28–29 June 2018, pp 875–879. Doi: https://doi.org/10.1109/PowerAfrica.2018.8520985.

Nakamura S, Ebihara Y, Fujita S, Goto T, Yamada N, Watari S, Omura Y (2018) Time domain simulation of geomagnetically induced current (GIC) flowing in 500-kV power grid in Japan including a three-dimensional ground inhomogeneity. Space Weather 16(12):1946–1959. https://doi.org/10.1029/2018SW002004

Nomura R, Shiokawa K, Pilipenko V, Shevtsov B (2011) Frequency-dependent polarization characteristics of Pc1 geomagnetic pulsations observed by multipoint ground stations at low latitudes. J Geophys Res 116:A01204. https://doi.org/10.1029/2010JA015684

NERC (2012) Effects of geomagnetic disturbances on the bulk power system. North American Electric Reliability Corp.

NERC (2017) TPL-007–2-Transmission system planned performance for geomagnetic disturbance events. North American Electric Reliability Corp.

Oyedokun D, Heys M, Cilliers, P, Gaunt CT (2020) Frequency components of geomagnetically induced currents for power system modeling. Paper presented at 2020 International SAUPEC/RobMech/PRASA Conference, Cape Town, South Africa, 29–31 January 2020, pp 1–6. doi: https://doi.org/10.1109/SAUPEC/RobMech/PRASA48453.2020.9041021.

Pirjola R (1985) On currents induced in power transmission systems during geomagnetic variations. IEEE Power Eng Rev PER. 5(10):42–43. https://doi.org/10.1109/MPER.1985.5528697

Pulkkinen A, Pirjola R, Viljanen A (2007) Determination of ground conductivity and system parameters for optimal modeling of geomagnetically induced current flow in technological systems. Earth Planets Space 59:999–1006. https://doi.org/10.1186/BF03352040

Pulkkinen A, Bernabeu E, Eichner J, Beggan C, Thomson AWP (2012) Generation of 100-year geomagnetically induced current scenarios. Space Weather 10:S04003. https://doi.org/10.1029/2011SW000750
Saito T (1969) Geomagnetic pulsations. Space Sci Rev 10(3):319–412. https://doi.org/10.1007/BF00203620
Torta JM, Serrano L, Regue JR, Sanchez AM, Roldan E (2012) Geomagnetically induced currents in a power grid of northern Spain. Space Weather 10(6):S06002. https://doi.org/10.1029/2012SW000793
Trivedi NB, Vitorello I, Kabata W, Dutra SLG, Padilha AL, Bologna MS, de Padua MB, Soares AP, Luz GS, FdeA P, Pirjola R, Viljanen A (2007) Geomagnetically induced currents in an electric power transmission system at low latitudes in Brazil: a case study. Space Weather 5(4):S04004. https://doi.org/10.1029/2006SW000282
Viljanen A, Pirjola R (1989) Statistics on geomagnetically-induced currents in the Finnish 400 kV power system based on recordings of geomagnetic variations. J Geomag Geoelectr 41:411–420. https://doi.org/10.5636/jgg.41.411
Watari S, Kunitake M, Kitamura K, Hori T, Kikuchi T, Shiokawa K, Nishitani N, Kataoka R, Kamide Y, Aso T, Watanabe Y, Tsuneta Y (2009) Measurements of geomagnetically induced current in a power grid in Hokkaido. Japan Space Weather 7(3):S03002. https://doi.org/10.1029/2008SW000417
Weigel RS, Cilliers PJ (2019) An evaluation of the frequency independence assumption of power system coefficients used in geomagnetically induced current estimates. Space Weather 17(12):1674–1688. https://doi.org/10.1029/2019SW002234

Publisher's Note